batteries

MDPI

Article

Understanding Heat Generation of LNMO Cathodes in Lithium-Ion Batteries via Entropy and Resistance

Kevin Böhm [1,*], Aleksandr Kondrakov [2], Torsten Markus [1] and David Henriques [1]

[1] Technische Hochschule Mannheim, Institute for Materials Science and Engineering (IMaSE), Paul-Wittsack-Straße 10, 68163 Mannheim, Germany; t.markus@hs-mannheim.de (T.M.); d.henriques@hs-mannheim.de (D.H.)
[2] BASF SE, Carl-Bosch-Straße 38, 67056 Ludwigshafen, Germany; aleksandr.kondrakov@basf.com
* Correspondence: k.boehm@hs-mannheim.de

Abstract

The heat generation of lithium-ion batteries is a critical parameter, as it significantly affects cell temperature. Poor thermal management can lead to elevated cell temperatures, accelerating side reactions, reducing cell lifetime, and, in extreme cases, causing thermal runaway. Therefore, understanding heat generation is crucial for the commercialization of emerging battery materials. Due to its high energy density, lithium–nickel–manganese–oxide (LNMO) is an attractive candidate for next-generation cathode materials; however, the composition of its heat generation is not yet fully understood. To address this, the state-of-charge (SoC)-dependent entropy coefficient and resistance of disordered LNMO cathodes are determined using the potentiometric method. The results show that both values are strongly influenced by the redox reactions of Ni and Mn. The entropy coefficient varies between 5.2 and -32.4 J mol^{-1} K^{-1}, depending on the SoC. Furthermore, the resistance exhibits a switching dependence on kinetics and mass transfer. The resulting heat flux calculations indicate that, at SoC < 20%, heat generation is dominated by the kinetic behavior of LNMO, leading to two exothermal peaks during discharge and one exothermal peak during charge. This behavior is validated through a comparison with a low-current calorimetric measurement.

Keywords: lithium-ion batteries; heat generation; entropy coefficient; state of charge (SoC); LNMO cathode; potentiometric method; thermal behavior; calorimetry; exothermal effects; endothermal effects

check for updates

Academic Editor: Xianglin Li

Received: 15 August 2025
Revised: 11 September 2025
Accepted: 24 September 2025
Published: 28 September 2025

Citation: Böhm, K.; Kondrakov, A.; Markus, T.; Henriques, D. Understanding Heat Generation of LNMO Cathodes in Lithium-Ion Batteries via Entropy and Resistance. *Batteries* **2025**, *11*, 357. https://doi.org/10.3390/batteries11100357

Copyright: © 2025 by the authors. Licensee MDPI, Basel, Switzerland. This article is an open access article distributed under the terms and conditions of the Creative Commons Attribution (CC BY) license (https://creativecommons.org/licenses/by/4.0/).

1. Introduction

The cell temperature is one of the most important factors in a lithium-ion battery (LIB), as it significantly impacts the cell capacity, cycle life, and safety [1,2]. Therefore, thermal management systems need to be implemented to maintain the optimal operating temperature of LIBs, which is typically between 20 °C and 40 °C [3,4], while maintaining a temperature variation below 5 K in the battery modules [3]. Since, at low temperatures, lithium plating and sluggish transport mechanisms hinder cell performance and, at elevated temperatures, side reactions and the threat of potential thermal runaway increase [5,6], it is crucial to efficiently adapt these management systems. To design an effective thermal management system, the heat generation of the cells must be well understood.

While state-of-the-art cathode systems such as nickel–cobalt–manganese (NCM) [7–14] and lithium–iron–phosphate (LFP) [8,11–13] have already been extensively investigated

in experimental studies and simulations, new battery materials like lithium–nickel–manganese–oxide (LNMO) lack a comprehensive description of heat generation. LNMO is a potential candidate for next-generation cathode materials for LIBs due to its high operating potential of ~4.7 V (vs. Li/Li^+), which theoretically enables specific energies of about 650 Wh kg^{-1} in half-cell configuration against lithium metal [15–17]. In practical full-cell configurations, LNMO/graphite systems deliver about 265 Wh kg^{-1}, comparable to NCM/graphite (250–300 Wh kg^{-1}) and around 25% higher than LFP/graphite (≈210 Wh kg^{-1}) [18,19]. Moreover, unlike NCM, it does not contain cobalt, which has been criticized for its environmental and social impacts and significantly increases cathode costs [17,20]. Depending on the preparation of the active material, LNMO can exist in an ordered spinel structure ($P4_332$) or a disordered spinel structure ($Fd\bar{3}m$) [17]. For disordered LNMO, improved efficiency and cycle life is reported [21]. Nevertheless, LNMO in general suffers from severe degradation mechanisms, such as electrolyte decomposition due to high voltages and parasitic side reactions [22,23], especially at elevated temperatures [23,24]. Moreover, an increased capacity loss is reported for elevated temperatures [25,26]. This underscores the necessity of understanding the heat generation of LNMO cathodes.

The description of heat generation in lithium-ion batteries (LIBs) during cycling can be traced back to Bernardi et al. [27], who decomposed the total heat flux $\dot{Q}_{total}$ into four contributions: the reversible heat flux $\dot{Q}_{rev}$, the irreversible heat flux $\dot{Q}_{irrev}$, the heat of mixing $\dot{Q}_{mix}$, and the heat flux due to parasitic side reactions $\dot{Q}_{par}$. This relationship is expressed as

$$\dot{Q}_{total} = \dot{Q}_{rev} + \dot{Q}_{irrev} + \dot{Q}_{mix} + \dot{Q}_{par}. \tag{1}$$

Due to its minor contribution to heat generation for cycling C-rates below 1 h^{-1}, $\dot{Q}_{mix}$ is often neglected [28,29]. It describes the heat absorption or generation due to the formation and relaxation of concentration gradients inside the active materials [28–30]. As a result, it also contributes to heat generation shortly after the current is shut off.

Another heat flux source that can be neglected when cycling the cells post-formation and under standard operation conditions is $\dot{Q}_{par}$ [29]. This is caused by unfavorable side reactions that do not directly contribute to the energy storage of the cell, such as the formation of the solid electrolyte interphase (SEI).

This leaves $\dot{Q}_{rev}$ and $\dot{Q}_{irrev}$ as the most significant heat sources in lithium-ion batteries (LIBs) during cycling [29,31]. Their combined contribution can be approximated as

$$\dot{Q}_{total} \approx \dot{Q}_{rev} + \dot{Q}_{irrev}, \tag{2}$$

where $\dot{Q}_{irrev}$ results from ohmic resistance and polarization and is always exothermic. These same effects also cause the voltage U during the charge or discharge of the cell to deviate from the cell's open-circuit voltage U_{OCV}, leading to an overpotential. This overpotential can be used to calculate the irreversible heat flux as

$$\dot{Q}_{irrev} = I(U - U_{OCV}) = I^2 R_{total}, \tag{3}$$

where I is the current, and R_{total} is the total resistance of the cell under the applied conditions. To understand the origin of R_{total}, the overpotential can be separated into three components, each reflecting a distinct contribution to the overall resistance. The ohmic resistance R_{Ohm} and its overpotential η_{Ohm} primarily arise from the bulk electrolyte, separator, and current collector [32,33]. The overpotential $\eta_{Concentration}$ arises from lithium transport driven by concentration gradients, both in the electrolyte near the electrode surface [34] and within the electrode [35]. For illustration, while the Li-ion diffusion coefficient in a common electrolyte such as LP40 is on the order of 10^{-7} cm^2 s^{-1} [36], solid-state lithium diffusion in

LNMO is several orders of magnitude lower (typically 10^{-9} to 10^{-12} cm^2 s^{-1} [37]), making solid-state diffusion within the active material the dominant contribution to the concentration resistance $R_{Concentration}$ of the cell. Finally, the activation overpotential $\eta_{Activation}$ and transfer resistance $R_{Transfer}$ are a result of the kinetics at the electrolyte/electrode interface of the cells [34], where a small $R_{Transfer}$ resembles a faster electrode reaction. The total resistance can thus be expressed as the sum of the individual contributions derived from the three overpotentials:

$$R_{total} = \frac{\eta_{Ohm} + \eta_{Concentration} + \eta_{Activation}}{I} = R_{Ohm} + R_{Concentration} + R_{Transfer}. \quad (4)$$

For LNMO, values of the ohmic resistance [37], diffusion coefficient [22,37–42], and transfer resistance [37,40,43] have been reported in the literature, determined using the galvanostatic intermittent titration technique (GITT) and electrochemical impedance spectroscopy (EIS). While the ohmic resistance remains relatively constant, the diffusion coefficient and transfer resistance exhibit a significant state-of-charge (SoC) dependence. As a result, the diffusion coefficient shows minima during the redox reactions of Ni and Mn, and the transfer resistance increases rapidly at a low SoC. A more detailed discussion of the corresponding literature data is provided in Section 3.3.

The reversible heat flux $\dot{Q}_{rev}$ is generated by entropy changes in the electrodes, which occur due to the lithiation and delithiation of the electrode material [29]. As different phase transitions and lithiation mechanisms take place, the entropy change strongly depends on the electrode materials used and the SoC of the cells [44–46]. To calculate this, it is essential to determine the entropy coefficient, dU_{OCV}/dT, which describes the variation in U_{OCV} as a function of temperature T. The reversible heat flux is then given by

$$\dot{Q}_{rev} = IT\frac{dU_{OCV}}{dT} = IT\frac{\Delta S}{nF}, \quad (5)$$

linking the entropy coefficient directly to the entropy change ΔS, the number of transferred electrons n (for LNMO: $n = 1$), and the Faraday constant F. Rearranging this relationship yields the expression for the entropy change:

$$\Delta S = nF\frac{dU_{OCV}}{dT}. \quad (6)$$

For $Li_xNi_{0.5}Mn_{1.5}O_4$, the entropy change was determined in the literature. Jobst et al. [15] analyzed ordered $Li_xNi_{0.5}Mn_{1.5}O_4$ ($P4_332$) over the full lithiation range from 4.9 V to 1.5 V, utilizing the redox reaction of Mn for charge. They observed two negative segments associated with the redox reactions of Ni and two positive segments associated with the Mn reactions. Mao et al. [47], on the other hand, determined the entropy changes for disordered $Li_xNi_{0.5}Mn_{1.5}O_4$ ($Fd\bar{3}m$) within a voltage range of 4.95 V to 3.5 V, where Ni is the primary redox-active species. They also observed a negative entropy coefficient with a two-segment characteristic. However, at a low SoC, they detected a decline in the entropy coefficient, leading to a significant endothermal peak during discharge and an exothermal peak during charge.

When reviewing the existing literature on the heat generation of LNMO cathodes, it was found that some studies investigated the heat flux at C-rates of 1 h^{-1} or higher. Sayah et al. [48] analyzed the heat flux by charging and discharging LNMO half-cells at a C-rate of 1 h^{-1}. They observed a relatively constant heat flux for most of the charge and discharge steps. However, toward the end of the constant current phase of charge and discharge, an increase in heat flux was detected, which was significantly higher for the discharge curve. Baazizi et al. [49] reported increased heat generation during discharge compared to charge.

Moreover, they observed an increase in heat generation with an increasing C-rate, whereas the heat generation during charge remained consistently low. This might be connected to the low capacity retention at elevated C-rates during charge. For C-rates of 1 h^{-1} and 1.5 h^{-1}, a segment-like behavior of the heat flux during discharge and charge was observed, while a significant exothermal heat flux peak at low SoCs was detectable.

So far, a comprehensive analysis that integrates all relevant contributions to heat generation in LNMO cathodes is lacking, leaving the origin of the characteristic SoC-dependent heat flux largely unexplained. Therefore, the aim of this study was to resolve the composition of heat generation in $Li_xNi_{0.5}Mn_{1.5}O_4$ by linking heat flux to the fundamental properties of reversible and irreversible heat. To achieve this, the entropy change was determined using the potentiometric method. Additionally, the resistance was estimated from the voltage drop at each SoC step during the measurement. Based on these values, the reversible and irreversible heat fluxes were calculated as functions of the SoC. Finally, the sum of these heat fluxes was compared to low-current calorimetric measurements to characterize the heat generation behavior of disordered LNMO.

2. Materials and Methods

2.1. Cell Preparation

The active materials, electrolyte, cell housings, and separators used in this study were provided by BASF SE (Ludwigshafen, Germany). The supplied $Li_xNi_{0.5}Mn_{1.5}O_4$ electrode sheets, coated on an aluminum foil, had an areal capacity of 2 mAh cm^{-2} according to the supplier. As the electrolyte, 100 µL of Selectilyte LP 40 was used. Electrodes with a diameter of 15 mm were punched from these sheets inside an argon-filled glovebox, maintaining O_2 and H_2O levels below 0.5 ppm. Whatman GF/D with a diameter of 17 mm served as the separator. For the counter electrode, lithium with a diameter of 13 mm and a thickness of 0.5 mm was used (Nanografi Nano Technology, Ankara, Türkiye). After cell stacking, the cell housing was sealed under a pressure of 1 ton.

Following cell assembly, each cell was placed on a PAT-Stand-16 (EL-Cell GmbH, Hamburg, Germany) with a 3E-Coin-to-PAT-Adapter (EL-Cell GmbH, Hamburg, Germany). To achieve constant temperatures, the setup was placed inside an IPP55plus temperature chamber (Memmert GmbH + Co.KG, Schwabach, Germany) set to 25 °C. Moreover, the PAT-Stand-16 was connected to a BCS-805 battery cycler (BioLogic, Seyssinet-Pariset, France). To determine the current used in the potentiometric measurement, the cells were first rested for 3 h inside the temperature chamber. Then, the cells were charged with a constant-current (CC) and constant-voltage (CV) phase. After this first charge, the cells were discharged and charged again once. The settings of the battery cycler are displayed in Table 1. The current used corresponds to a C-rate of 1/10 h^{-1} for an areal capacity of 2 mAh cm^{-2}.

Table 1. Potentiostat settings for the initialization cycle of LNMO half-cells after assembly.

Parameter	Value
Voltage limits	3.5–4.8 V
Current	±0.353 mA
Cut-off current	0.035 mA
Time limit CV	30 min

During the second charging step, the capacity was determined. Based on this capacity, the current I_{step} used in the potentiometric measurement was calculated (C-rate: 1/20 h^{-1}). In total, five cells were prepared, divided into two groups. Group one consisted of three cells, and group two consisted of two cells. The two groups underwent slightly different

measurement protocols, which are referred to in the following as Measurement 1 (M1) and Measurement 2 (M2). The determined capacities of the used cells are listed in Table 2.

Table 2. Cell capacities and resulting currents used for the potentiometric measurement at a C-rate of $1/20\ h^{-1}$.

Measurement	Cell	Capacity [mAh]	Areal Capacity [mAh cm^{-2}]	I_{step} [mA]
M1	Cell 1	4.136	2.341	0.207
	Cell 2	4.160	2.354	0.208
	Cell 3	4.076	2.307	0.204
M2	Cell 4	4.247	2.403	0.212
	Cell 5	4.177	2.364	0.209
Mean		4.159 ± 0.063	2.354 ± 0.035	

2.2. Determination of the Entropy Coefficient

After the initial setup, the three cells (cells 1–3) of M1 were placed in three universal battery holders from Gamry Instruments (Warminster, PA, USA). The holders were positioned inside a second IPP55plus temperature chamber to maintain the required temperature variations. A VMP-300 potentiostat from BioLogic (Seyssinet-Pariset, France) was used for charging, discharging, and voltage measurements.

First, the temperature chamber was set to 25 °C, and the cells were charged at a constant current of $1/10\ h^{-1}$. Once a voltage of 4.8 V was reached, a CV phase was applied for 30 min or until the minimum limiting current of 0.035 mA was undershot.

To determine the entropy coefficient of the LNMO cathodes, the potentiometric method was chosen. This method has already been demonstrated in various studies on cathode materials such as LFP [50], lithium–manganese–iron–phosphate (LMFP) [51], lithium–manganese–oxide (LMO) [52], lithium- and manganese-rich layered composite cathodes (LMR) [46], lithium–nickel–cobalt–aluminum–oxide (NCA) [46], and NCM [46,53], as well as on anode materials, such as graphite [44,53], lithium–titanate–oxide (LTO) [51], and silicon [54]. The measurement was subdivided into several discharging and charging steps, leading to stepwise lithiation or delithiation of the electrode. Figure 1 demonstrates the resulting voltage signal of cell 1 due to the stepwise discharge.

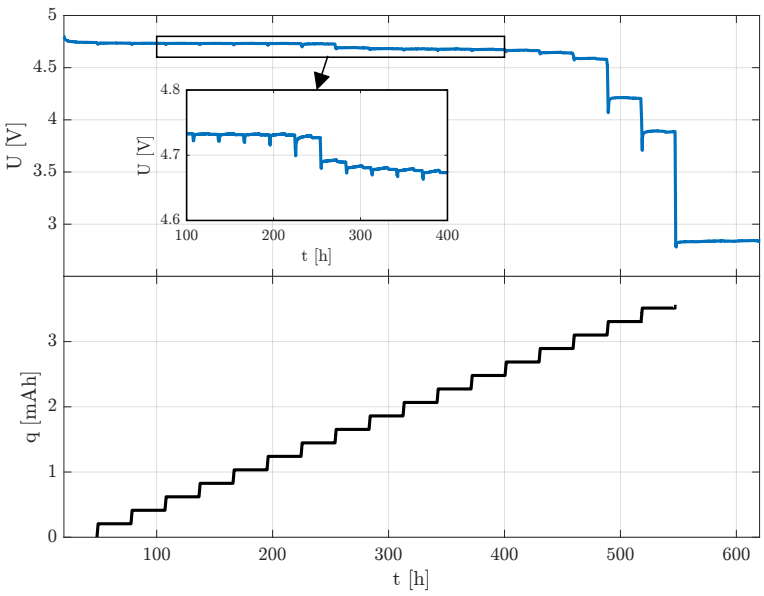

Figure 1. Voltage signal and discharge capacity of cell 1 during the potentiometric measurement.

The corresponding SoC of each step was calculated based on the maximum discharge capacity $q_{d,max}$ and the maximum charge capacity $q_{c,max}$:

$$SoC_d = (1 - \frac{q_d}{q_{d,max}}) \cdot 100\%, \tag{7}$$

$$SoC_c = \frac{q_c}{q_{c,max}} \cdot 100\%. \tag{8}$$

Each SoC step consists of four segments, which are shown in Figure 2. The first segment of a step is the charging or discharging of the cell. Therefore, a constant current of 1/20 h^{-1} (Table 2) is applied for one hour, a low C-rate to enable equilibrium and stable relaxation.

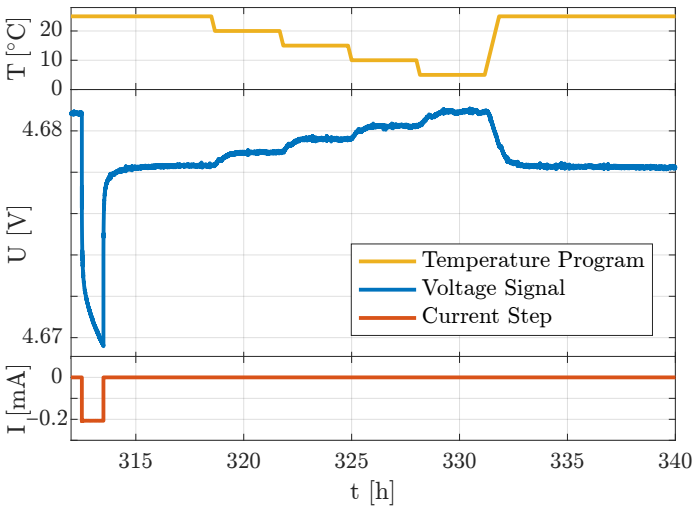

Figure 2. Schematic demonstration of one SoC step of the potentiometric measurement during discharge/lithiation.

In the second segment, the cell voltage relaxes. An open-circuit voltage (OCV) phase is applied for approximately 6 h during discharge and 8 h during charge. The variation in relaxation time results from a desynchronization between the temperature chamber and the potentiostat. The third segment involves temperature variation. During this segment, the temperature chamber cools down in 5 °C steps. Each cooldown is performed at a rate of −0.5 K/min and takes 10 min. Each temperature is maintained for 3 h. The set temperatures are 25 °C, 20 °C, 15 °C, 10 °C, and 5 °C. Finally, the temperature chamber is heated back to 25 °C at a rate of 0.5 K/min. During this segment, the potentiostat remains in the OCV phase. Finally, the fourth segment consists of an OCV phase until the next SoC step is initiated.

A linear fit was applied between the final voltage signal at 25 °C before the temperature variation started and the first point where the voltage signal returned to the baseline at 25 °C to minimize the impact of residual voltage shifts. This linear fit was then subtracted from the voltage signal, bringing the voltage value at 25 °C close to zero.

For each temperature step, the resulting voltage value was obtained by calculating the mean of the voltage values in the 10 min before the next temperature change. Subsequently, the voltage values for each temperature were plotted, as shown in Figure 3. The resulting slope of the linear voltage data fit was then used to calculate the entropy coefficient according to Equation (6), with $n = 1$.

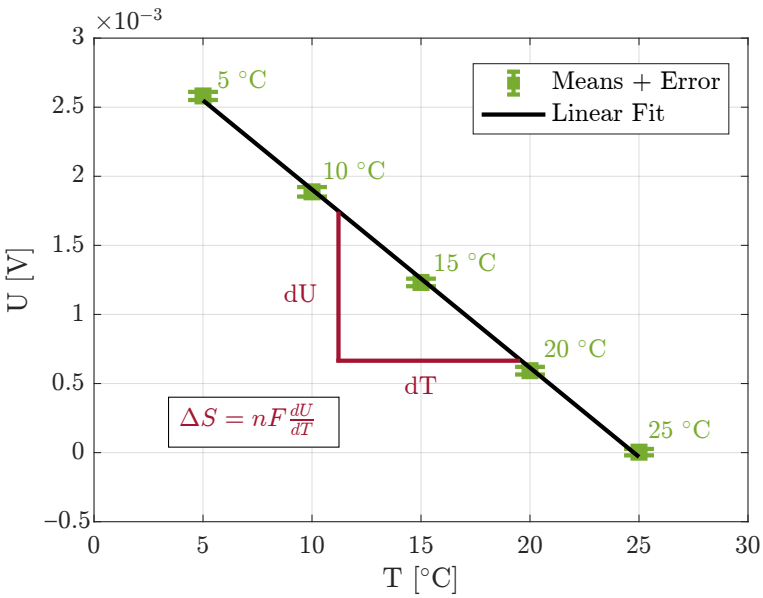

Figure 3. Schematic demonstration of one SoC step of the potentiometric measurement.

To increase the number of measurement points below 20% SoC, two additional cells were prepared, and the potentiometric protocol was adjusted accordingly. The adapted protocol is referred to as M2.

To shorten the measurement time, the cells were discharged at a current of 1/20 h^{-1} for 16 h. Afterward, the stepwise discharge with temperature variation was initiated. The measurement parameters remained the same as for the first set of cells, except that the duration of one current step was reduced from 1 h to 0.5 h, and the relaxation time before the temperature measurement was extended to 24 h to achieve smaller SoC steps of about 2.5% instead of 5% as in M1, thereby enabling the detection of short-term SoC-dependent changes in resistance and entropy. Moreover, the longer relaxation ensures a more complete equilibration. Significant differences in the entropy between M1 and M2 in this region may therefore also indicate insufficient relaxation in M1, providing a self-consistency check of the results. For SoC values above 20%, however, an extension of the relaxation was not necessary, since sufficient equilibration was already achieved in this range, as confirmed by the good agreement between the individual cells. In addition, this region is characterized not by short-term changes but rather by two pronounced plateaus, which is why no reduction in the current step duration was required.

To facilitate comparison and improve the traceability of the two measurement protocols M1 and M2, flowcharts for both discharge/lithiation and charge/delithiation are provided in Appendix A (Figures A1 and A2).

2.3. Resistance Analysis

To determine the resistance of the cells during each SoC step, the relaxation curve of the second segment from the potentiometric measurement is used. From this segment, the maximal difference between the voltage of the end of the charge/discharging step and the relaxation voltage ΔU_{max}, along with the step current I_{step} and the ohmic law, is used to calculate the resistance R_{total}:

$$R_{total} = \frac{\Delta U_{max}}{I_{step}}. \tag{9}$$

The calculated resistance resembles the sum of all resistances (see Equation (4)) due to the specific applied current at the specific temperature of 25 °C.

2.4. Isothermal Calorimetry

To validate the measured entropy coefficient and resistance of the cells, three coin cells were cycled inside an MMC 274 calorimeter (NETZSCH-Gerätebau GmbH, Selb, Germany) equipped with a high-temperature coin cell module. The calorimeter was placed inside a cooling incubator, a KB 240 E6 (BINDER GmbH, Tuttlingen, Germany). The incubator was set to 5 °C with a 40% fan speed.

The cells were treated similarly to those used for entropy determination, undergoing an initial discharge and charge in a Memmert temperature chamber. The cycling parameters were identical. Inside the calorimeter, the cells rested for 3 h to allow the system to reach a steady state at the set measurement temperature of 25 °C. The cells were then charged at a C-rate of 1/10 h^{-1}, based on a capacity of 2 mAh cm^{-2}, until they reached the upper voltage limit of 4.8 V, followed by a CV phase. After an additional rest period of 0.5 h, the cells were cycled at a C-rate of 1/10 h^{-1}, again based on 2 mAh cm^{-2}, beginning with a discharge step. Between discharge and charge, the cells were rested for 0.5 h to allow the calorimeter signal to stabilize.

A low C-rate (1/10 h^{-1}) was selected because both concentration and charge transfer resistances are current-dependent. At higher rates, the irreversible heat flux could not be reliably separated from the calorimeter baseline signal, whereas at 1/10 h^{-1}, the measured flux remains interpretable and consistent with the resistance-based calculations.

At certain points of the data processing, MATLAB coding was supported with the assistance of OpenAI's ChatGPT-4o (San Francisco, CA, USA) to improve code readability and implementation. All code was reviewed and validated by the authors.

3. Results and Discussion

3.1. Intercalation Steps

To identify the SoC positions of the reaction steps during discharge and charge, the voltage curves of all five cells are shown in Figure 4. In agreement with the literature [55], three distinct voltage segments can be observed for disordered LNMO: one at approximately 4.7 V, a second at 4.65 V, and a third at 4.0 V. Table 3 links these reaction steps to the corresponding reduction and oxidation reactions.

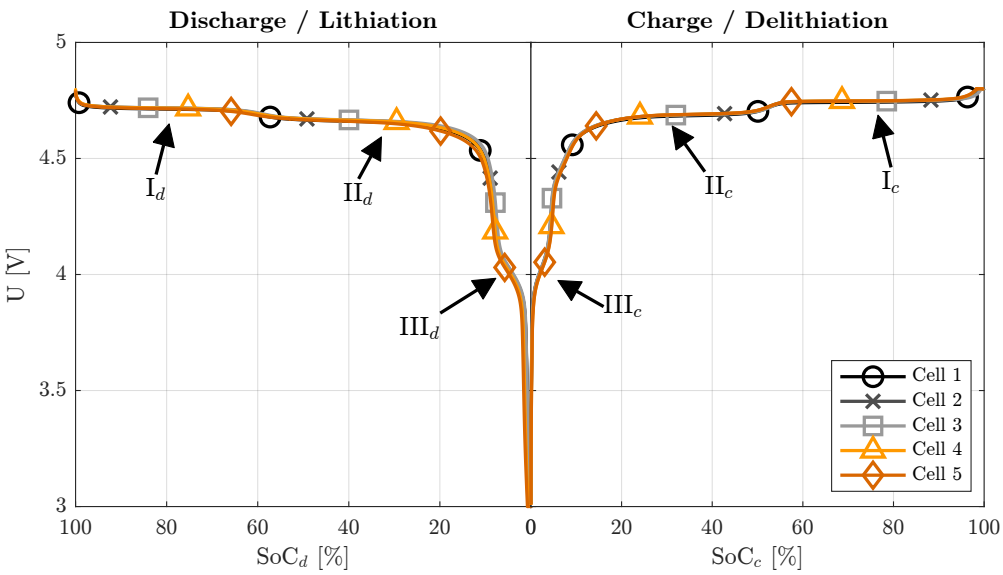

Figure 4. Discharge and charge curves of all five LNMO half-cells showing excellent overlap, enabling a reliable comparison based on the SoC. Three distinct voltage regions are visible, linking the SoC to the corresponding intercalation steps summarized in Table 3.

All three segments can be observed during both charge and discharge. However, segment III_c is less pronounced during charging, causing the two nickel redox steps to extend over a broader SoC range and to shift toward lower SoC_c values.

Table 3. Identified redox reaction steps of the LNMO cathode, as reported in the literature [56–58]. The corresponding $SoC_{d/c}$ ranges were determined in this work from the voltage profile shown in Figure 4.

Reaction Step	Reduction/Oxidation	$SoC_{d/c}$ Range [%]
I_d	$Ni^{4+} \rightarrow Ni^{3+}$	60–100
II_d	$Ni^{3+} \rightarrow Ni^{2+}$	17–60
III_d	$Mn^{4+} \rightarrow Mn^{3+}$	0–17
III_c	$Mn^{3+} \rightarrow Mn^{4+}$	0–12
II_c	$Ni^{2+} \rightarrow Ni^{3+}$	12–51
I_c	$Ni^{3+} \rightarrow Ni^{4+}$	51–100

3.2. Entropy Coefficient

Figure 5 presents the results for the two measurements. The black line represents a fit for the first measurement, which includes cells 1–3 and was conducted over the entire SoC range of the cell. The orange line corresponds to cells 4 and 5, for which the potentiometric measurement was performed only at low SoC values.

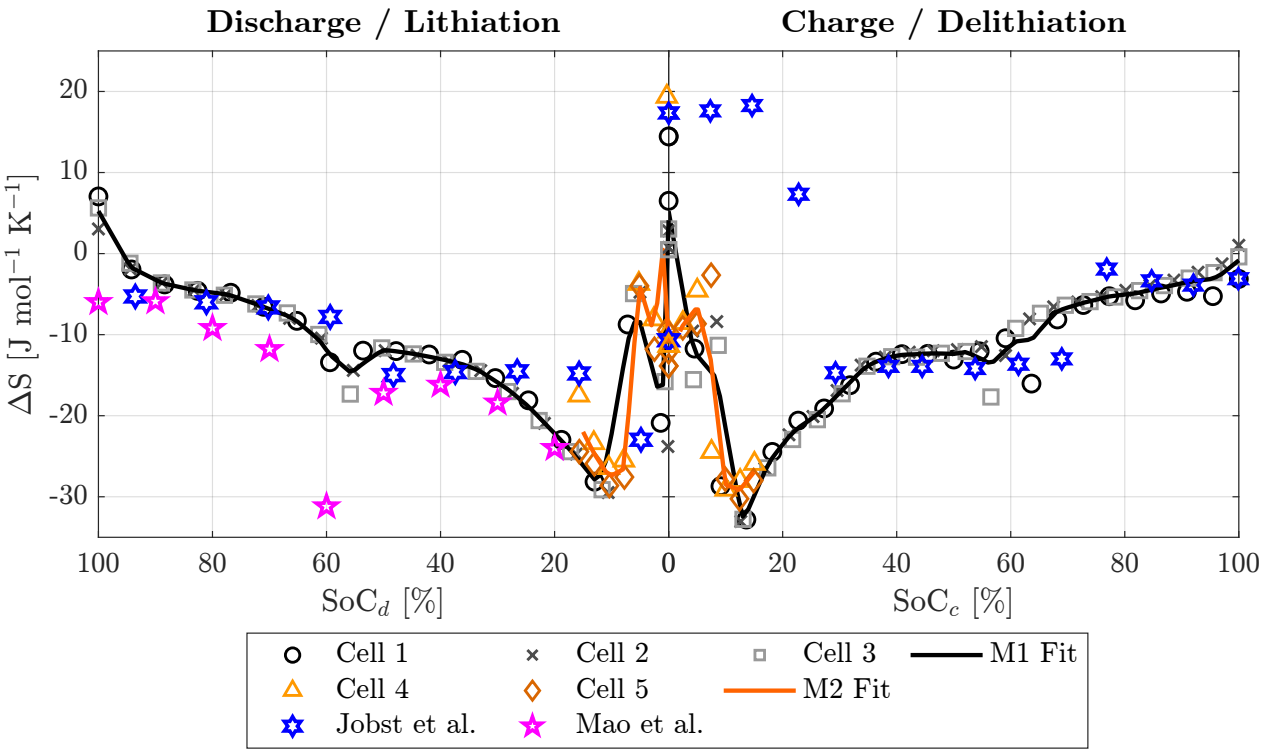

Figure 5. The SoC-dependent entropy change for LNMO cathodes. While this work (black and orange) and Mao et al. [47] (magenta) examined disordered LNMO, Jobst et al. [15] (blue) analyzed ordered LNMO. For improved readability, the y-axis is limited to -35 J mol^{-1} K^{-1}, cutting off the ΔS values reported by Mao et al. for an SoC_d below 20 %, which range from -269 J mol^{-1} K^{-1} to -92 J mol^{-1} K^{-1}. Literature data adapted with permission from [15]. Copyright 2023 American Chemical Society.

The entropy coefficient exhibits a stepwise behavior that coincides with the reaction steps of the voltage signal (Table 3). Table 4 lists the entropy changes for several SoC_d values during discharge. An initial zero crossing is observed, caused by an initial drop

from approximately 5.2 J mol^{-1} K^{-1} to about −3.2 J mol^{-1} K^{-1}. The following segment is attributed to the first Ni reaction.

Between the first and second Ni reactions, a local minimum of approximately −14.5 J mol^{-1} K^{-1} is observed at around 56% SoC$_d$, indicating a brief increase in entropy change. The subsequent segment, starting at approximately −11.9 J mol^{-1} K^{-1}, gradually decreases until it reaches the absolute minimum of the entropy coefficient at 13% SoC$_d$, with a value of about −27.9 J mol^{-1} K^{-1}. After this minimum, a stepwise increase in the entropy coefficient is observed. The individual cells exhibit values up to 15 J mol^{-1} K^{-1}, while the fit reaches a maximum of only 4.1 J mol^{-1} K^{-1}. The steep incline is interrupted by a short decrease in the entropy coefficient at approximately 2% SoC$_d$, possibly caused by the Mn reaction step. This behavior is observed in both measurements.

However, the minima in the second measurement tend to shift toward lower SoC$_d$ values due to the initial continuous discharge step. Nevertheless, the minimum value of −27.4 J mol^{-1} K^{-1} is in good agreement with the first measurement. In contrast, the value at 0% SoC$_d$ exhibits a final decrease compared to M1, which contradicts the initial trend. Since no specific reaction occurs that could explain this behavior, the final value at 0% SoC$_d$ in M2 should be regarded critically.

Table 4. Entropy values of the fit curve for LNMO half-cells during discharge. Arrows indicate whether the data point corresponds to a local minimum (↓) or maximum (↑). Since extrema of the fitted curve are shown, the step size deviates from the regular interval.

M1			M2		
SoC$_d$ [%]	**ΔS [J mol^{-1} K^{-1}]**	**Local Extrema**	**SoC$_d$ [%]**	**ΔS [J mol^{-1} K^{-1}]**	**Local Extrema**
100	5.2 ± 2.1	↑			
90	−3.2 ± 0.1				
80	−4.8 ± 0.1				
70	−6.8 ± 0.2				
60	−11.9 ± 1.0				
56	−14.5 ± 2.4	↓			
50	−11.9 ± 0.3	↑			
40	−13.0 ± 0.4				
30	−15.9 ± 0.4				
20	−22.2 ± 0.3				
13	−27.9 ± 0.4	↓	15	−22.0 ± 4.0	↑
10	−22.2 ± 4.4		10	−27.4 ± 1.6	↓
5	−8.5 ± 4.4	↑	5	−4.2 ± 0.2	↑
2	−16.4 ± 3.3	↓	3	−8.8 ± 2.1	↓
0	4.1 ± 2.1	↑	0	−10.9 ± 1.8	↑

The entropy change observed by Mao et al. [47] matches the Ni segments at high and medium SoC$_d$ values. Nevertheless, the results presented in this study are, on average, about 3.5 J mol^{-1} K^{-1} higher. Furthermore, the decrease in entropy during the transition between segments is more pronounced in the data reported by Mao et al. Below 20% SoC$_d$, Mao et al. observed a sharp drop to a minimum of −269 J mol^{-1} K^{-1}, which is approximately ten times lower than the values measured in this work. However, Mao et al. noted that these values are subject to a large error margin due to instabilities in the OCV baseline and suggested that differences may also arise from material-related effects, such as the Mn^{3+}/Mn^{4+} redox system. Notably, the pronounced entropy minima and the associated heat peaks reported in their study were not observed in other works [48,49] or in the present measurements.

Another study by Jobst et al. [15] measured the entropy coefficient of ordered LNMO, again showing matching values for the entropy change during the Ni segments. Furthermore, the observed minimum of approximately −23 J mol^{-1} K^{-1} was followed by a stepwise increase to positive values. This observation coincides with the results of this study.

However, neither study observed the small drop caused by the Mn segment for disordered LNMO.

The entropy change during charge appears to be approximately mirrored with respect to 0% SoC when compared to the discharge profile. The according charge values are listed in Table 5. The absolute minimum at 13% SoC$_c$, reaching about −32.4 J mol^{-1} K^{-1}, is about −4.5 J mol^{-1} K^{-1} smaller than that observed during discharge. The entropy values for the two Ni reaction steps are in good agreement with the discharge values at around −12 J mol^{-1} K^{-1} and −5 J mol^{-1} K^{-1}. However, the local minimum between the two reaction steps is less precisely represented by the fit, as the minima of the individual cells are slightly shifted to approximately 60 ± 5% SoC$_c$. Nevertheless, a local minimum of approximately −15 J mol^{-1} K^{-1} can also be assumed here, as indicated by the individual cell measurements.

Table 5. Entropy values of the fit curve for LNMO half-cells during charge. Arrows indicate whether the data point corresponds to a local minimum (↓) or maximum (↑). Since extrema of the fitted curve are shown, the step size deviates from the regular interval.

M1			M2		
SoC$_c$ [%]	**ΔS [J mol^{-1} K^{-1}]**	**Local Extrema**	**SoC$_c$ [%]**	**ΔS [J mol^{-1} K^{-1}]**	**Local Extrema**
0	5.2 ± 8.0	↑	5	−6.9 ± 2.2	↑
10	−21.6 ± 6.9		10	−28.2 ± 1.1	
13	−32.4 ± 0.2	↓	12	−29.0 ± 1.2	↓
20	−23.6 ± 0.8				
30	−17.2 ± 0.6				
40	−12.6 ± 0.2				
50	−12.4 ± 0.7				
52	−12.1 ± 0.5	↑			
56	−13.4 ± 3.1	↓			
60	−11.4 ± 0.4				
70	−6.7 ± 0.7				
80	−5.1 ± 0.5				
90	−3.7 ± 1.0				
100	−0.8 ± 2.2	↑			

A comparison with the values of the change in entropy for ordered LNMO, determined by Jobst et al. [15], shows good agreement with the results of this study for the Ni segments. However, the results of their work showed a more constant entropy value for each segment, while the results of this work show steady decreases toward lower SoC$_c$ values. For charge, their results showed an initial segment at low SoC$_c$. This difference to our results could be caused by inaccuracies by reading the graphs of Jobst et al. and by the different lower discharging limit. They discharged the cells to 1.5 V, which correlates to a lithiation state of $Li_{2.5}Ni_{0.5}Mn_{1.5}O_4$, fully utilizing the redox reaction of Mn, while the voltage limit of 3.0 V used in this study limits the main redox reactions to Ni. As a result, the initial segment of Jobst et al. during charge is explained by a new intermediate phase of $Li_{1.5}Ni_{0.5}Mn_{1.5}O_4$.

3.3. Resistance

Figure 6 shows the SoC-dependent resistance of the LNMO half-cells. For discharge (Table 6) and charge (Table 7), a "W" shape is observed.

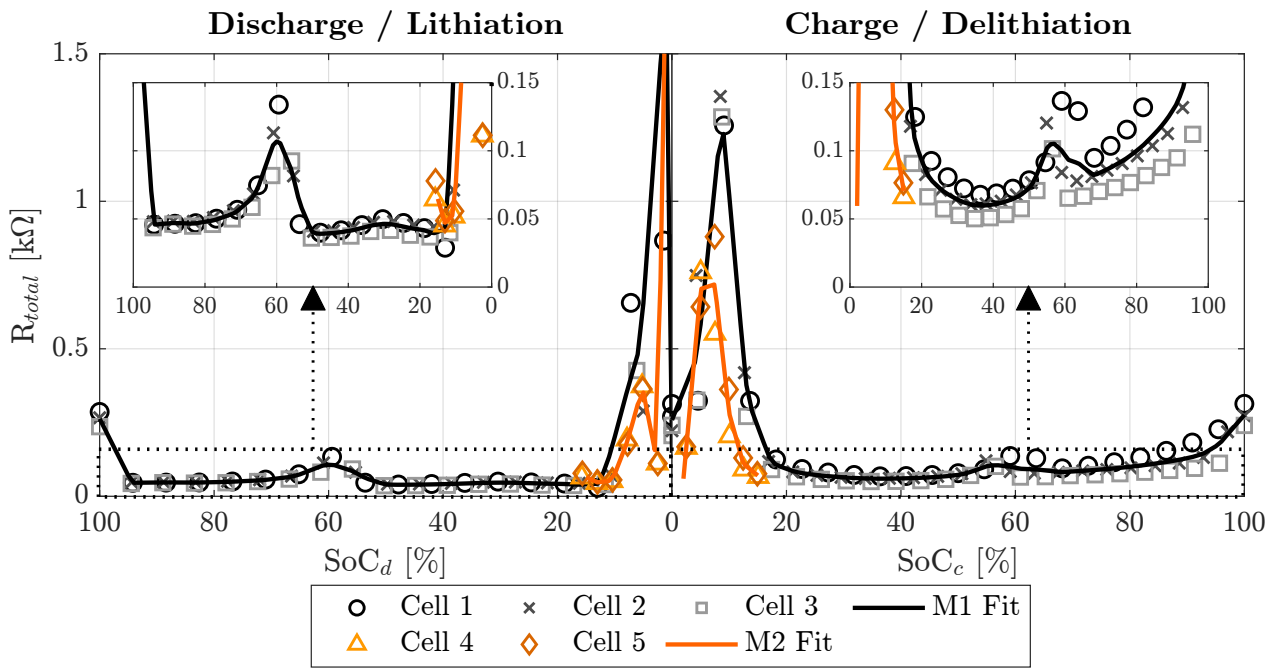

Figure 6. SoC-dependent total resistance of the LNMO cathodes, determined from the potentiometric measurements M1 (black) and M2 (orange).

Table 6. Resistance of the fit curve for LNMO half-cells during discharge. Arrows indicate whether the data point corresponds to a local minimum (↓) or maximum (↑). Since extrema of the fitted curve are shown, the step size deviates from the regular interval.

M1			M2		
SoC_d [%]	R_{total} [Ω]	Local Extrema	SoC_d [%]	R_{total} [Ω]	Local Extrema
100	262.7 ± 25.2	↑			
94	45.9 ± 2.2	↓			
90	46.8 ± 1.5				
80	47.9 ± 2.2				
70	58.0 ± 3.8				
60	106.8 ± 21.7	↑			
50	40.4 ± 3.9				
48	39.1 ± 2.7	↓			
40	41.1 ± 3.4				
30	46.3 ± 4.4	↑			
20	42.2 ± 4.2		15	64.7 ± 8.3	
16	39.6 ± 4.8	↓	10	75.8 ± 3.0	
10	201.4 ± 134.6		5	351.6 ± 0.8	↑
1	1677.5 ± 993.2	↑	3	156.4 ± 6.2	↓
0	147.5 ± 160.6		0	1820.9 ± 16.7	↑

For the discharge, an initial resistance drop from approximately 262.7 Ω to about 45.9 Ω is observed. During reaction step I_d, the resistance remains relatively constant until a local maximum of approximately 106.8 Ω occurs at around 60% SoC_d. This peak correlates with the voltage shift between reaction steps I_d and II_d.

In reaction step II_d, a resistance segment is observed again, with resistance values tending to be lower than those in step I_d. At low SoC_d (<20% SoC_d), a rapid increase in resistance is observed in both measurements. However, in M1, a single peak is observed with a large standard deviation at the maximum value. In M2, the standard deviation is reduced, and two peaks are observed.

The minimum between these two peaks is located at approximately 3% SoC_d. It is assumed that this minimum is caused by reaction step III_d, which is not captured for M1 due to the SoC step width.

Table 7. Resistance of the fit curve for LNMO half-cells during charge. Arrows indicate whether the data point corresponds to a local minimum (↓) or maximum (↑). Since extrema of the fitted curve are shown, the step size deviates from the regular interval.

M1			M2		
SoC_c [%]	**R_{total} [Ω]**	**Local Extrema**	**SoC_c [%]**	**R_{total} [Ω]**	**Local Extrema**
0	258.7 ± 48.1		5	682.7 ± 65.5	
9	1228.3 ± 12.3	↑	7	715.5 ± 170.8	↑
10	1020.4 ± 45.6		10	286.7 ± 107.1	
20	93.3 ± 18.0		12	142.6 ± 38.8	
30	64.2 ± 11.4				
36	59.8 ± 9.1	↓			
40	60.6 ± 8.7				
50	72.6 ± 7.5				
57	105.1 ± 9.7	↑			
60	96.8 ± 33.6				
68	82.2 ± 13.8	↓			
70	84.2 ± 14.0				
80	100.0 ± 23.6				
90	129.4 ± 43.0				
100	275.6 ± 36.7	↑			

As for the change in entropy, the general shape of the resistance over SoC_c appears to be mirrored at 0% SoC. However, at low SoC_c, both M1 and M2 exhibit only a single peak, reaching approximately 1228.3 Ω in M1 and 715.5 Ω in M2. This could be caused by the less distinct Mn reaction step III_c compared to III_d, which was not captured by any of the SoC steps. As a result, the presence of a peak at very low (<5%) SoC_c values is still assumed but is expected to have a lower impact.

For SoC_c > 20%, the two resistance segments corresponding to Ni reaction steps II_c and I_c can be observed, separated by a local maximum of approximately 105.1 Ω at around 57% SoC_c. Again, it can be seen that the resistance values for II_c are lower than those for I_c. However, both steps exhibit resistance values approximately 1.5 to 2 times higher than the discharge segments. At the end of the charge, the resistance again reaches a local maximum of 275.6 Ω, which is in good agreement with the initial resistance observed during the discharge step.

As previously described, the resistance obtained in this study corresponds to the total resistance as defined in Equation (4). The literature provides a comprehensive overview of the contributing mechanisms, enabling an explanation of the observed resistance curve.

First, concentration resistance results from low lithium diffusion, whose main parameter is the diffusion coefficient D_{Li^+}. Reported values for D_{Li^+} range from 10^{-9} to 10^{-12} cm^2 s^{-1} [39–42]. Figure 7 summarizes the SoC-dependent diffusion coefficients for charge and discharge as reported in various literature sources. According to these studies, D_{Li^+} exhibits three minima during both discharge and charge. The minimum below

20% $SoC_{d/c}$ is attributed to Mn reaction step III. This minimum appears as a sharp peak, which would coincide with reported resistance observations and explains the difficulty in capturing a measurement point at this peak using the potentiometric method.

The second minimum, occurring between approximately 20% $SoC_{d/c}$ and 60% $SoC_{d/c}$, is caused by Ni reaction step II, while the third minimum, between 60% $SoC_{d/c}$ and 100% $SoC_{d/c}$, is linked to Ni reaction step I. In all studies, D_{Li^+} during step I is lower than D_{Li^+} during step II. This correlates with the findings on resistance, where a lower resistance was observed during step II than during step I for both discharge and charge. Moreover, Versaci et al. [22] reported lower D_{Li^+} values during charge than during discharge. This finding again aligns with resistance trends, where the resistance during steps I and II is higher for charge than for discharge.

However, at the SoC extremes and at the transition between reaction steps, the literature data show that D_{Li^+} increases, whereas in our measurements, the resistance also increases. This behavior cannot be explained by concentration resistance, since an increase in D_{Li^+} would typically result in a decrease in resistance.

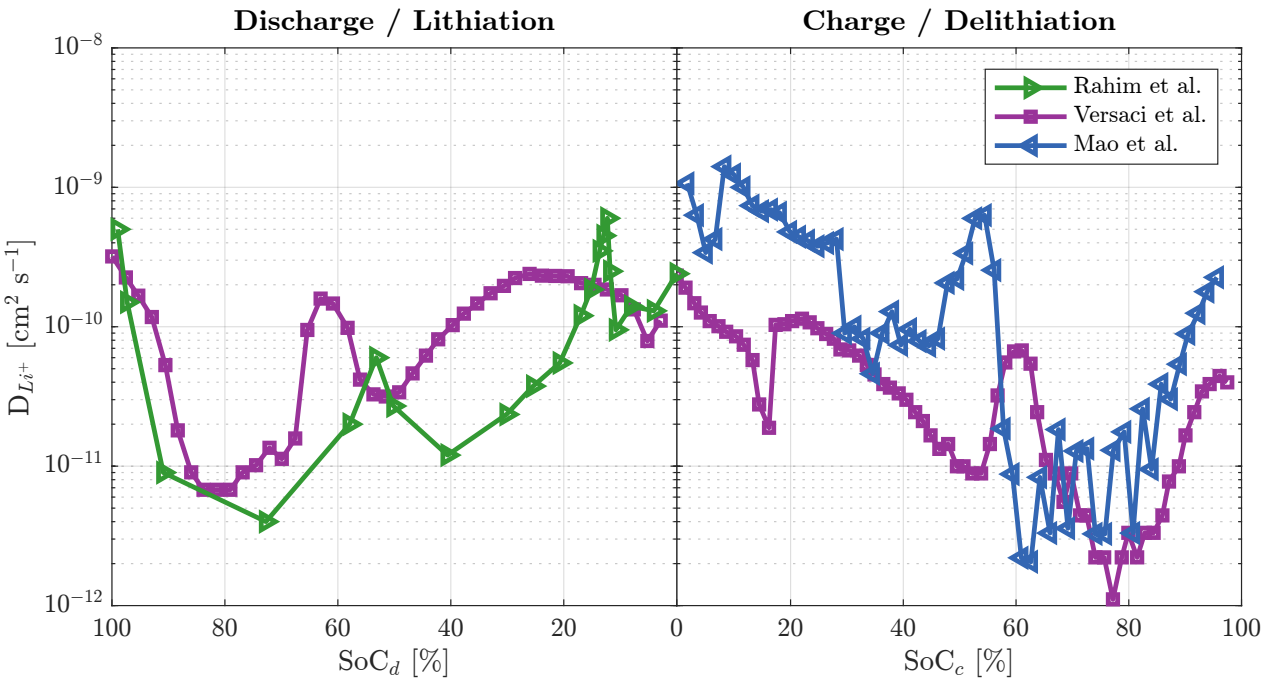

Figure 7. Diffusion coefficient for disordered $Li_xNi_{0.5}Mn_{1.5}O_4$ during discharge/ lithiation from the literature: Rahim et al. [41] (green), Versaci et al. [22] (magenta), and Mao et al. [39] (blue). Literature data adapted with permission from [39]. Copyright 2016 American Chemical Society. Data from [22] reproduced with permission from the respective authors.

For the ohmic resistance, Amin et al. [37] reported no significant changes during charge. However, their reported transfer resistance exhibits a significant increase, reaching up to 500 Ω for an SoC_c below 10%. This resistance increase decreases significantly at higher SoC_c values. This observation aligns well with our previously reported findings on resistance behavior during charge, where an initial peak that is not caused by diffusion can be seen. Similar observations were made by Mohamedi et al. [40], who reported an increase in transfer resistance below 4.6 V and above 4.72 V. This indicates that, at the SoC extremes, the rising diffusion coefficient reduces concentration resistance, while the increasing charge transfer resistance becomes the main contributor to the total cell resistance.

While the literature does not provide information on transfer resistance between reaction steps or during discharge, the total resistance follows the same trend as during charge. The total resistance increases when the concentration resistance decreases. Consequently,

during the transitions between reaction steps, kinetics appear to be the limiting factor, leading to an increase in resistance. In contrast, during the reaction steps, mass transport is the limiting factor. This implies that kinetic limitations may also underlie the other total resistance peaks in LNMO (Figure 6), extending the interpretation beyond the low-SoC_c region suggested by Amin et al. [37].

3.4. Heat Generation

To compare the measured values of the change in entropy and the resistance, the resulting heat flux for a C-rate of 1/10 h^{-1} and a cell temperature of 25 °C is calculated using the mean measured values. Figure 8 shows the reversible heat flux according to Equation (5) and the irreversible heat flux according to Equation (3). The calculations are performed for both measurements, with the black line corresponding to the results from M1 and the orange line corresponding to those from M2.

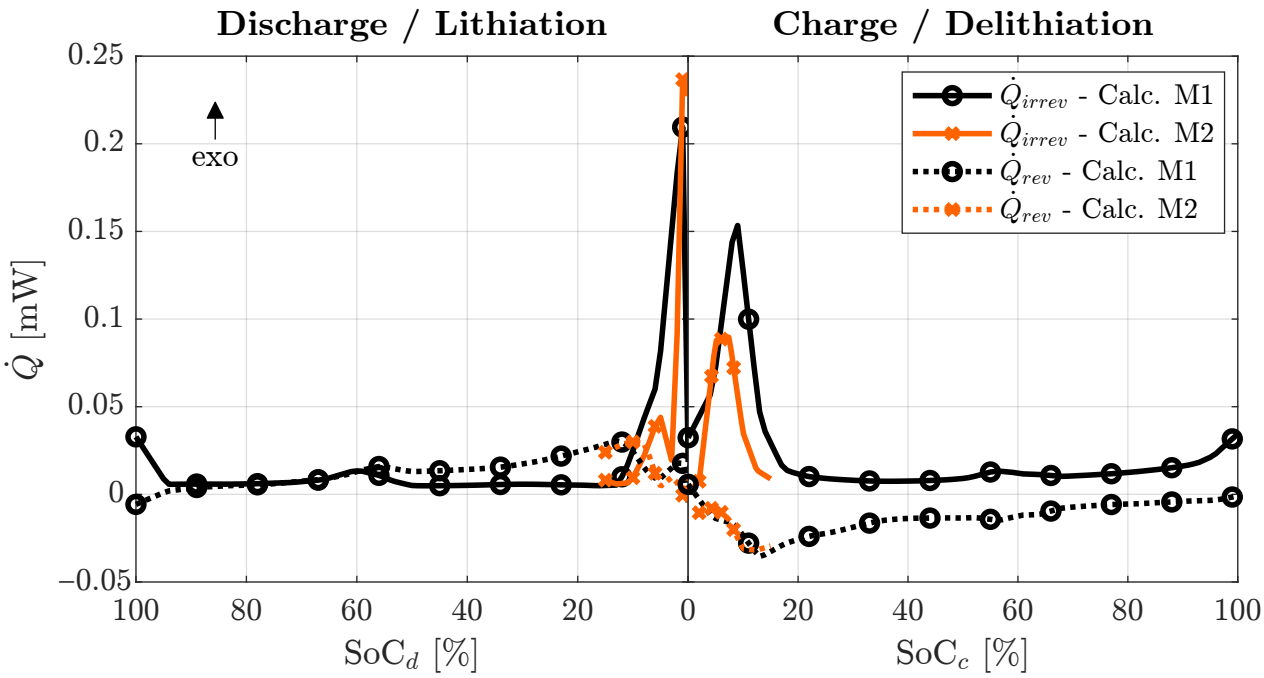

Figure 8. Reversible and irreversible heat flux for LNMO calculated from the mean values for M1 (Calc. 1, black) and M2 (Calc. 2, orange). For the calculations, a temperature of 25 °C and a C-rate of 1/10 h^{-1} were used.

The irreversible heat flux is, as expected, constantly exothermal. The curve follows the trend of the resistance. The reversible heat flux, on the other hand, shows a dependency on discharge or charge, which agrees with its reversible nature. During discharge, except for a short initial endothermal minimum, a constantly exothermal heat flux is calculated. While it remains nearly identical to the irreversible heat flux during Ni reaction step I_d, it exceeds the irreversible heat flux during Ni reaction step II_d. Moreover, it shows an increasing trend until it reaches approximately 10% SoC_d. From there on, the reversible heat flux decreases rapidly, while the irreversible heat flux increases. This behavior is observed in both calculations.

During charge, an initial irreversible heat flux peak is observed in both calculations, followed by a relatively constant low exothermal irreversible heat flux. In both cases, the reversible heat flux decreases until it reaches an SoC_c of approximately 10%. A negative value corresponds to an endothermal heat flux, indicating that, at around 10% SoC_c, the highest amount of heat is absorbed. Afterward, the heat flux declines until it is close to

0 mW when fully charged. Throughout the entire charging process, the reversible heat flux remains endothermal.

The observation of the reversible heat flux being endothermal during charge and exothermal during discharge is in agreement with the calculations made by Mao et al. [47]. However, due to the rapid decrease in the entropy coefficient below 20% SoC, their calculations predicted a strong endothermal and exothermal peak in this range. This contrasts with the present calculations, which show a reduction in reversible heat due to a decrease in the entropy coefficient.

By neglecting the heat of mixing and parasitic side reactions, the total heat generation during cycling can be calculated as the sum of reversible and irreversible heat flux. The resulting total heat flux for M1 and M2 is displayed in Figure 9.

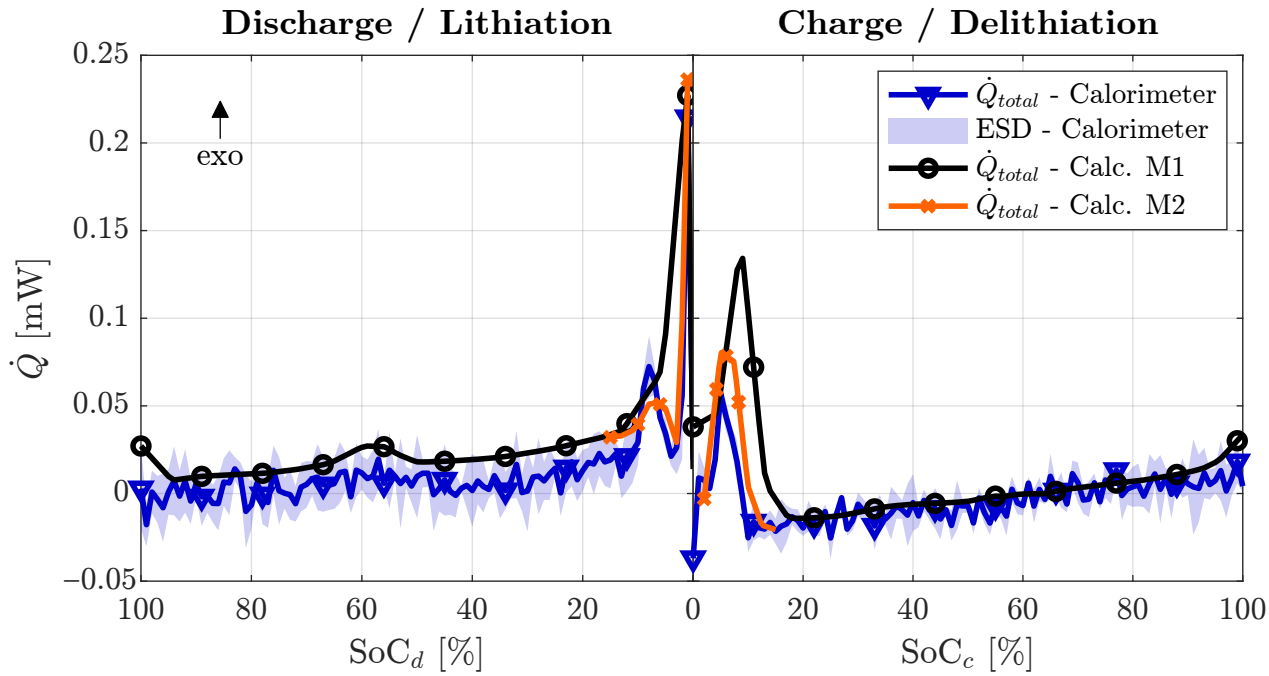

Figure 9. Comparison of the total heat flux of disordered $Li_xNi_{0.5}Mn_{1.5}O_4$ cathodes during discharge and charge between the calculations (M1—black; M2—orange) and a calorimetric measurement. For both the calculations and the measurement, a C-rate of 1/10 h^{-1} and an isothermal temperature of 25 °C were applied. The calorimetric measurement represents the mean of three smoothed coin cell measurements. The estimated standard deviation (ESD) is calculated from the standard deviation of these three measurements.

The blue line in Figure 9 corresponds to the heat flux measurement in a calorimeter under the same conditions as those used for the calculations. While the absolute values of the measurements should be interpreted with caution due to the very low heat flux signal, the overall trend allows for a meaningful comparison. A good agreement between the heat flux curves during charge and discharge is observed.

During discharge, calculation M1 predicts an initial drop in the heat flux, followed by a small exothermal segment caused by the first Ni reaction I_d. At approximately 56% SoC_d, a local maximum is calculated, followed by a second segment, which increases as the SoC_d decreases. This increase in heat flux is mainly driven by the reversible heat flux. A similar trend is observed in the calorimeter measurements, where a slight decrease in heat flux for the second segment compared to the first segment can also be observed due to the reduced irreversible heat flux of Ni reaction II_d.

The first deviations in the curve progression between calculation M1 and the calorimeter measurements are observed for SoC_d values below 20%. While calculation M1 predicts

a rapid increase in heat flux, the increase in the calorimetric measurement is interrupted by a minimum at approximately 2% SoC_d, followed by another sharp increase in heat flux during the final SoC_d percentages. However, calculation M2 also shows this drop in heat flux, reinforcing the earlier assumption that this behavior might be primarily caused by a reduction in resistance due to Mn reaction step III_d. This reaction step is not captured for M1 due to a larger step width.

As a result, for the discharge of disordered LNMO cathodes, a relatively flat heat flux between 100% and 20% SoC_d can be confirmed, followed by a strong increase in heat flux due to the increase in resistance, forming a distinct double peak for low C-rates.

For higher C-rates ($\geq$1 h^{-1}), a similar double-peak shape was still observed by Sayah et al. [48], whereas Baazizi et al. [49] reported only a single peak at the position of the double peak, which, with increasing C-rate, merged into one broad peak due to the loss of the characteristic plateaus and peaks caused by the higher current.

For charge, both calculations predict a single peak below 20% SoC_c. This is confirmed by the calorimeter measurement; however, the initial increase exhibits a minor interruption, which might be caused by Mn reaction step III_c, not captured due to the step width of the calculation.

The heat flux above 20% SoC_c shows a steady increase, starting as endothermal and becoming exothermal at approximately 60% SoC_c. This behavior is again primarily driven by the endothermal nature of the reversible heat flux. Notably, the exothermal peak of the irreversible heat flux at around 55% SoC_c appears to be neutralized by an endothermal peak of the reversible heat flux.

Finally, for both charge and discharge, the heat flux peak at 100% $SoC_{d/c}$ is not observed in the calorimeter measurements. This suggests that, at 100% $SoC_{d/c}$, the resistance is overestimated.

A direct comparison with Sayah et al. [48] is difficult because, in their study, the initial heat release during charge may be overlapped by the preceding discharge step due to the missing relaxation, and the first charge step can further be influenced by CEI formation. Baazizi et al. [49] likewise reported a single initial heat peak during charge, while at higher C-rates, the prolonged CV phase leads to reduced currents and, thus, an additional apparent initial peak. Overall, the comparability with the literature is limited due to differences in measurement protocols and boundary conditions.

4. Conclusions

In this study, the heat generation during the cycling of disordered $Li_xNi_{0.5}Mn_{1.5}O_4$ cathodes was examined with a focus on the reversible and irreversible heat flux.

To determine the reversible heat flux, the change in entropy was measured using the potentiometric method. The change in entropy ranged from approximately 5 J mol^{-1} K^{-1} to −32.5 J mol^{-1} K^{-1}, being mostly negative. Moreover, the reaction steps of Ni and Mn were reflected in the variations in the entropy. Based on the obtained entropy values, the calculation of the reversible heat flux resulted in exothermal heat flux during discharge and endothermal heat flux during charge.

The irreversible heat flux was predicted by estimating the resistance from the potential drop while using the potentiometric method. The determined resistance was the sum of ohmic resistance, transfer resistance, and concentration resistance, leading to a characteristic resistance curve for disordered $Li_xNi_{0.5}Mn_{1.5}O_4$. A comparison with the literature indicated that the resistance during the reaction steps was primarily driven by concentration resistance due to limited diffusion. On the other hand, distinct resistance peaks were observed at the transitions between reaction steps. By extending the findings to low-SoC states, these increases were assumed to be caused by an increase in transfer

resistance, leading to pronounced double peaks during discharge at SoC_d values below 20% and a distinct resistance peak during charge below 20% SoC_c.

The calculated total heat flux was compared to calorimetric measurements, which confirmed the determined curves for reversible and irreversible heat flux. Moreover, it was observed that, at low SoC values, the irreversible heat flux was dominant, whereas at medium and elevated SoC levels, the heat flux was significantly influenced by reversible heat. However, the calculations in this study were conducted for low currents only. As a result, the influence of the irreversible heat flux is expected to become more significant at higher currents [59].

Consequently, to fully predict the heat flux of disordered $Li_xNi_{0.5}Mn_{1.5}O_4$ cathodes, further investigation into concentration resistance and transfer resistance is necessary.

For practical applications, the results indicate that thermal management systems should be designed to accommodate rapid increases in heat flux when the SoC value drops below 20%. Alternatively, based on the current data, a potential strategy could be to program the battery management system to limit the current in this SoC range or avoid it by setting a lower voltage limit of approximately 4.5 V (vs. Li/Li^+). Furthermore, the findings suggest that the most effective heat flux optimization could be achieved by reducing the transfer resistance of LNMO cathodes.

Author Contributions: Conceptualization, K.B.; methodology, K.B. and D.H.; software, K.B.; validation, K.B.; formal analysis, K.B.; investigation, K.B.; resources, K.B., A.K., T.M. and D.H.; data curation, K.B.; writing—original draft preparation, K.B.; writing—review and editing, K.B., A.K., T.M., and D.H.; visualization, K.B.; supervision, T.M. and D.H.; project administration, A.K. and D.H.; funding acquisition, D.H. All authors have read and agreed to the published version of the manuscript.

Funding: The junior research group Kems4Bats is supported by the German Federal Ministry of Education and Research (BMBF, grant number 03XP0303) and by industry and science sponsors (Netzsch-Gerätebau GmbH, Comsol Multiphysics GmbH, MAHLE GmbH, Volkswagen AG, BASF SE, GHS Vakuumtechnik GmbH, Pfeiffer Vacuum GmbH, BorgWarner Inc., CHARISMA, Verfasste Studierendenschaft Hochschule Mannheim).

Data Availability Statement: The original contributions presented in this study are included in the article; further inquiries can be directed to the corresponding author.

Acknowledgments: For the publication fee, the authors acknowledge financial support from Technische Hochschule Mannheim. The authors also acknowledge the use of OpenAI's ChatGPT-4o (OpenAI, San Francisco, CA, USA) for assistance in grammar, spelling, and sentence structure checks, as well as for support in MATLAB coding. All outputs were reviewed and validated by the authors, who take full responsibility for the content of this publication.

Conflicts of Interest: Author A.K. was employed by the company BASF SE. The remaining authors declare that the research was conducted in the absence of any commercial or financial relationships that could be construed as a potential conflict of interest.

Appendix A

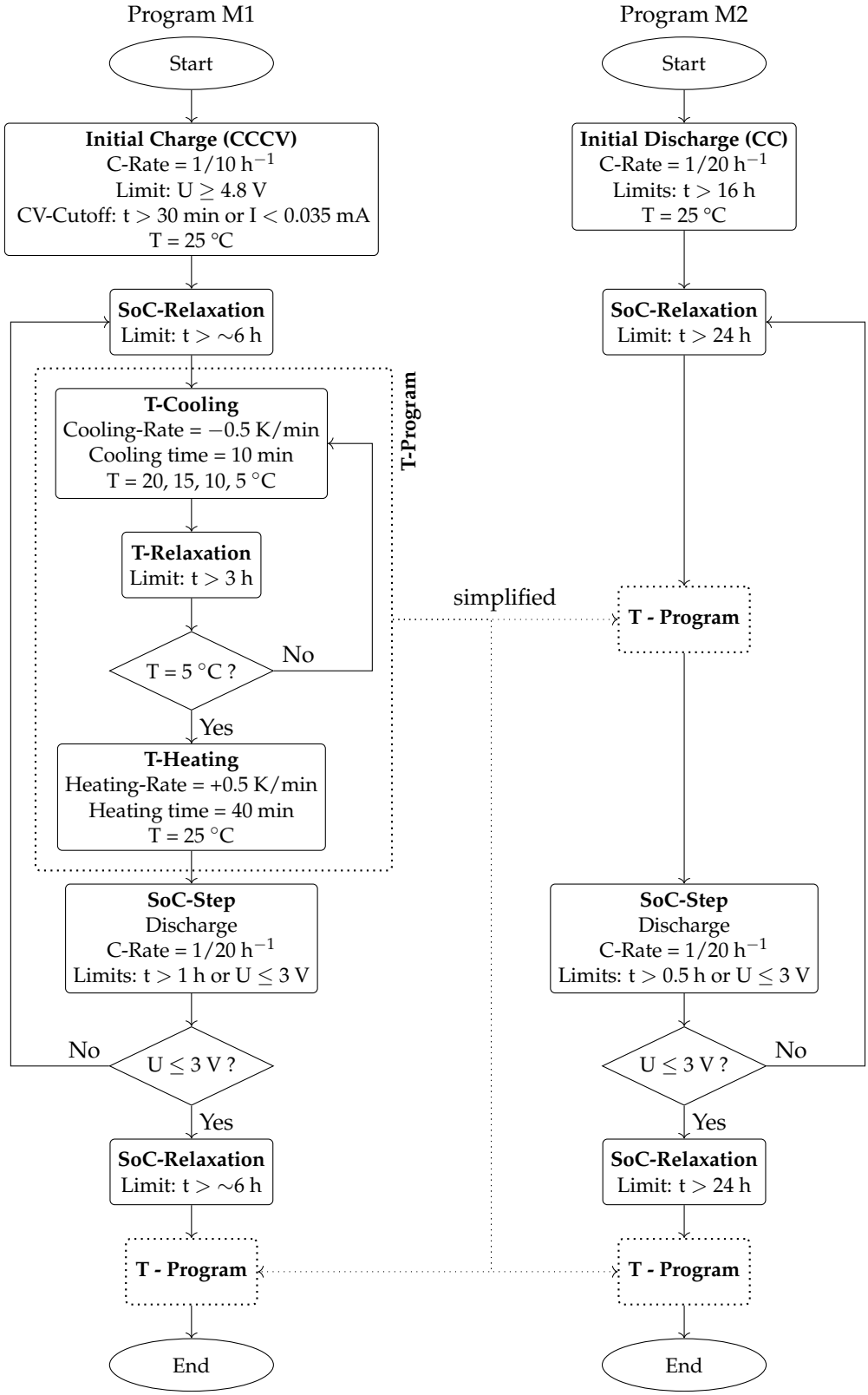

Figure A1. Comparison of the flowcharts for the two potentiometric protocols M1 (**left**) and M2 (**right**), both referring to the discharge/lithiation process. The temperature program is shown in detail only once, since its structure is identical in both protocols, to enhance clarity. Dotted lines indicate which steps are summarized into a single simplification block and where these simplifications have been applied.

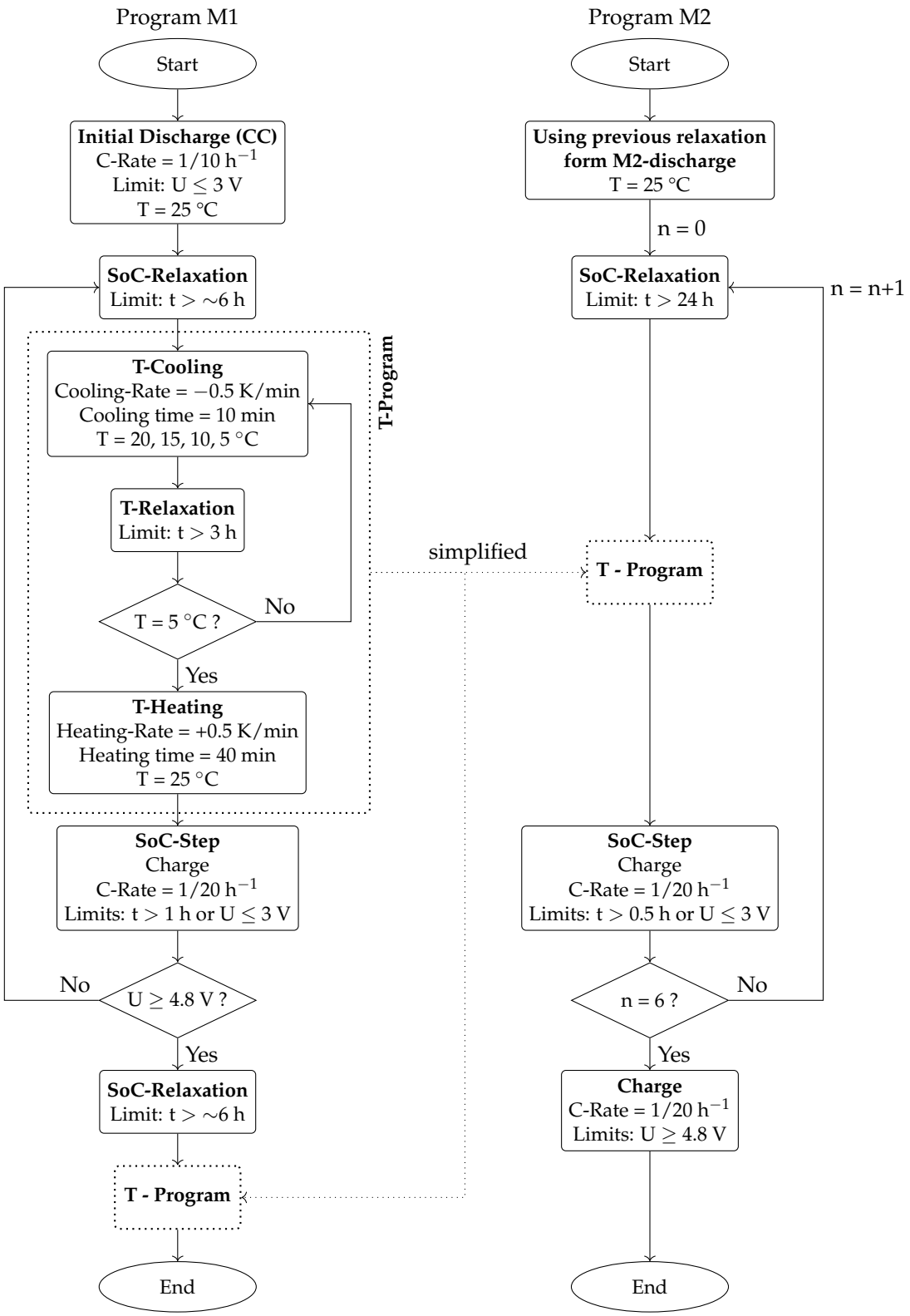

Figure A2. Comparison of the flowcharts for the two potentiometric protocols M1 (**left**) and M2 (**right**), both referring to the charge/delithiation process. The temperature program is shown in detail only once, since its structure is identical in both protocols, to enhance clarity. In protocol M2, no initial discharge step is included, as it directly follows the preceding M2 discharge program; the first temperature step is not evaluated due to the extended relaxation in the prior experiment. At $n = 6$ (≈30% SoC), the cell is fully charged to obtain the total capacity. Dotted lines indicate which steps are summarized into a single simplification block and where these simplifications have been applied.

References

1. Choudhari, V.G.; Dhoble, D.A.S.; Sathe, T.M. A review on effect of heat generation and various thermal management systems for lithium ion battery used for electric vehicle. *J. Energy Storage* **2020**, *32*, 101729 . [CrossRef]
2. Leng, F.; Tan, C.M.; Pecht, M. Effect of Temperature on the Aging rate of Li Ion Battery Operating above Room Temperature. *Sci. Rep.* **2015**, *5*, 12967. [CrossRef] [PubMed]
3. Pesaran, A.A. Battery thermal models for hybrid vehicle simulations. *J. Power Sources* **2002**, *110*, 377–382. [CrossRef]
4. Chen, K.; Chen, Y.; Li, Z.; Yuan, F.; Wang, S. Design of the cell spacings of battery pack in parallel air-cooled battery thermal management system. *Int. J. Heat Mass Transf.* **2018**, *127*, 393–401. [CrossRef]
5. Birkl, C.R.; Roberts, M.R.; McTurk, E.; Bruce, P.G.; Howey, D.A. Degradation diagnostics for lithium ion cells. *J. Power Sources* **2017**, *341*, 373–386. [CrossRef]
6. Zhang, Y.; Lu, Y.; Jin, J.; Wu, M.; Yuan, H.; Zhang, S.; Davey, K.; Guo, Z.; Wen, Z. Electrolyte Design for Lithium-Ion Batteries for Extreme Temperature Applications. *Adv. Mater.* **2024**, *36*, e2308484. [CrossRef]
7. Yang, J.; Zhang, H.; Xu, Y.; Li, P. Analysis of heat generation in lithium-ion battery components and voltage rebound based on electrochemical and thermal coupled model. *J. Energy Storage* **2023**, *72*, 108554. [CrossRef]
8. Lin, C.; Wang, F.; Fan, B.; Ren, S.; Zhang, Y.; Han, L.; Liu, S.; Xu, S. Comparative study on the heat generation behavior of lithium-ion batteries with different cathode materials using accelerating rate calorimetry. *Energy Procedia* **2017**, *142*, 3369–3374. [CrossRef]
9. Zhao, W.; Rohde, M.; Mohsin, I.U.; Ziebert, C.; Seifert, H.J. Heat Generation in NMC622 Coin Cells during Electrochemical Cycling: Separation of Reversible and Irreversible Heat Effects. *Batteries* **2020**, *6*, 55. [CrossRef]
10. Lyu, P.; Huo, Y.; Qu, Z.; Rao, Z. Investigation on the thermal behavior of Ni-rich NMC lithium ion battery for energy storage. *Appl. Therm. Eng.* **2020**, *166*, 114749. [CrossRef]
11. Jindal, P.; Katiyar, R.; Bhattacharya, J. Evaluation of accuracy for Bernardi equation in estimating heat generation rate for continuous and pulse-discharge protocols in LFP and NMC based Li-ion batteries. *Appl. Therm. Eng.* **2022**, *201*, 117794. [CrossRef]
12. Jiang, F.; Peng, P.; Sun, Y. Thermal analyses of $LiFePO_4$/graphite battery discharge processes. *J. Power Sources* **2013**, *243*, 181–194. [CrossRef]
13. Liu, S.; Lu, S.; Fu, Y.; Ma, W.; Zhang, H. In-situ measurement of the heat generation of LiFePO4 and $Li(Ni_{1/3}Co_{1/3}Mn_{1/3})O_2$ batteries. *J. Power Sources* **2023**, *574*, 233187. [CrossRef]
14. Tan, Y.; Li, Y.; Gu, Y.; Liu, W.; Fang, J.; Pan, C. Numerical Study on Heat Generation Characteristics of Charge and Discharge Cycle of the Lithium-Ion Battery. *Energies* **2023**, *17*, 178. [CrossRef]
15. Jobst, N.M.; Paul, N.; Beran, P.; Mancini, M.; Gilles, R.; Wohlfahrt-Mehrens, M.; Axmann, P. Dynamic Structure Evolution of Extensively Delithiated High Voltage Spinel $Li_{1+x}Ni_{0.5}Mn_{1.5}O_4 x < 1.5$. *J. Am. Chem. Soc.* **2023**, *145*, 4450–4461. [CrossRef]
16. Liang, G.; Peterson, V.K.; See, K.W.; Guo, Z.; Pang, W.K. Developing high-voltage spinel LiNi0.5Mn1.5O4 cathodes for high-energy-density lithium-ion batteries: Current achievements and future prospects. *J. Mater. Chem. A* **2020**, *8*, 15373–15398. [CrossRef]
17. Zhu, X.; Huang, A.; Martens, I.; Vostrov, N.; Sun, Y.; Richard, M.I.; Schulli, T.U.; Wang, L. High-Voltage Spinel Cathode Materials: Navigating the Structural Evolution for Lithium-Ion Batteries. *Adv. Mater.* **2024**, *36*, e2403482. [CrossRef] [PubMed]
18. Wentker, M.; Greenwood, M.; Leker, J. A Bottom-Up Approach to Lithium-Ion Battery Cost Modeling with a Focus on Cathode Active Materials. *Energies* **2019**, *12*, 504. [CrossRef]
19. Choi, S.; Feng, W.; Xia, Y. Recent Progress of High Voltage Spinel $LiMn_{1.5}Ni_{0.5}O_4$ Cathode Material for Lithium-Ion Battery: Surface Modification, Doping, Electrolyte, and Oxygen Deficiency. *ACS Omega* **2024**, *9*, 18688–18708. [CrossRef]
20. Mallick, S.; Patel, A.; Paranthaman, M.P.; Mugumya, J.H.; Kim, S.; Rasche, M.L.; Jiang, M.; Lopez, H.; Gupta, R.B. An overview of various critical aspects of low-cobalt/cobalt-free Li-ion battery cathodes. *Sustain. Energy Fuels* **2025**, *9*, 724–738. [CrossRef]
21. Wang, L.; Li, H.; Huang, X.; Baudrin, E. A comparative study of Fd-3m and P4332 "$LiNi_{0.5}Mn_{1.5}O_4$". *Solid State Ionics* **2011**, *193*, 32–38. [CrossRef]
22. Versaci, D.; Colombo, R.; Montinaro, G.; Buga, M.; Cortes Felix, N.; Evans, G.; Bella, F.; Amici, J.; Francia, C.; Bodoardo, S. Tailoring cathode materials: A comprehensive study on LNMO/LFP blending for next generation lithium-ion batteries. *J. Power Sources* **2024**, *613*, 234955. [CrossRef]
23. Kim, J.H.; Huq, A.; Chi, M.; Pieczonka, N.P.W.; Lee, E.; Bridges, C.A.; Tessema, M.M.; Manthiram, A.; Persson, K.A.; Powell, B.R. Integrated Nano-Domains of Disordered and Ordered Spinel Phases in LiNi0.5Mn1.5O4 for Li-Ion Batteries. *Chem. Mater.* **2014**, *26*, 4377–4386. [CrossRef]
24. Nisar, U.; Bansmann, J.; Hebel, M.; Reichel, B.; Mancini, M.; Wohlfahrt-Mehrens, M.; Hölzle, M.; Axmann, P. Borate modified Co-free LiNi0.5Mn1.5O4 cathode material: A pathway to superior interface and cycling stability in LNMO/graphite full-cells. *Chem. Eng. J.* **2024**, *493*, 152416. [CrossRef]
25. Ariyoshi, K.; Eguchi, M.; Hirooka, M. Correlation between capacity loss and increase in polarization in 5 V lithium-insertion material of $Li[Ni_{1/2}Mn_{3/2}]O_4$. *Solid State Ionics* **2021**, *371*, 115752. [CrossRef]

26. Liu, H.; Wang, J.; Zhang, X.; Zhou, D.; Qi, X.; Qiu, B.; Fang, J.; Kloepsch, R.; Schumacher, G.; Liu, Z.; et al. Morphological Evolution of High-Voltage Spinel $LiNi_{0.5}Mn_{1.5}O_4$ Cathode Materials for Lithium-Ion Batteries: The Critical Effects of Surface Orientations and Particle Size. *ACS Appl. Mater. Interfaces* **2016**, *8*, 4661–4675. [CrossRef] [PubMed]
27. Bernardi, D.; Pawlikowski, E.; Newman, J. A General Energy Balance for Battery Systems. *J. Electrochem. Soc.* **1985**, *132*, 5. [CrossRef]
28. Chalise, D.; Lu, W.; Srinivasan, V.; Prasher, R. Heat of Mixing During Fast Charge/Discharge of a Li-Ion Cell: A Study on NMC523 Cathode. *J. Electrochem. Soc.* **2020**, *167*, 090560. [CrossRef]
29. Ziebert, C.; Melcher, A.; Lei, B.; Zhao, B.; Rohde, M.; Seifert, H.J. Electrochemical—Thermal Characterization and Thermal Modeling for Batteries. In *Emerging Nanotechnologies in Rechargeable Energy Storage Systems*; Rodriguez-Martinez, L.M., Omar, N., Eds.; Micro and Nano Technologies; Elsevier Inc.: Amsterdam, The Netherlands, 2017; Book Section 6, pp. 195–229.
30. Mehta, R.; Gupta, A. Significance of heat of mixing analysed using a pseudo two-dimensional thermo-electrochemical model of lithium-ion cells. *Electrochim. Acta* **2024**, *475*, 143509. [CrossRef]
31. Maher, K.; Boumaiza, A.; Amin, R. Understanding the heat generation mechanisms and the interplay between joule heat and entropy effects as a function of state of charge in lithium-ion batteries. *J. Power Sources* **2024**, *623*, 235504. [CrossRef]
32. Choi, W.; Shin, H.C.; Kim, J.M.; Choi, J.Y.; Yoon, W.S. Modeling and Applications of Electrochemical Impedance Spectroscopy (EIS) for Lithium-ion Batteries. *J. Electrochem. Sci. Technol.* **2020**, *11*, 1–13. [CrossRef]
33. Xia, B.; Ye, B.; Cao, J. Polarization Voltage Characterization of Lithium-Ion Batteries Based on a Lumped Diffusion Model and Joint Parameter Estimation Algorithm. *Energies* **2022**, *15*, 1150. [CrossRef]
34. Wang, W.; Wei, X.; Choi, D.; Lu, X.; Yang, G.; Sun, C. Electrochemical cells for medium- and large-scale energy storage. In *Advances in Batteries for Medium and Large-Scale Energy Storage*; Woodhead Publishing: Cambridge, UK, 2015; pp. 3–28. [CrossRef]
35. Weppner, W.; Huggins, R.A. Determination of the Kinetic Parameters of Mixed-Conducting Electrodes and Application to the System Li_3Sb. *J. Electrochem. Soc.* **2022**, *124*, 1569–1578. [CrossRef]
36. Li, P.; Zhao, Z.; Fei, Y.; Zhang, H.; Li, G. $LiNO_3$-Based Electrolyte with Fast Kinetics for Lithium Metal Batteries Under Practical Conditions. *Adv. Energy Mater.* **2025**, *15*, 2500882. [CrossRef]
37. Amin, R.; Belharouak, I. Part-II: Exchange current density and ionic diffusivity studies on the ordered and disordered spinel $LiNi_{0.5}Mn_{1.5}O_4$ cathode. *J. Power Sources* **2017**, *348*, 318–325. [CrossRef]
38. Jobst, N.M.; Mancini, M.; Hölzle, M.; Wohlfahrt-Mehrens, M.; Axmann, P. Understanding the Low-Voltage Behavior of Stoichiometric Over Lithiated Spinel $Li_{1+x}Ni_{0.5}Mn_{1.5}O_4$: An Electrochemical Investigation. *J. Electrochem. Soc.* **2023**, *170*, 2. [CrossRef]
39. Mao, J.; Dai, K.; Xuan, M.; Shao, G.; Qiao, R.; Yang, W.; Battaglia, V.S.; Liu, G. Effect of Chromium and Niobium Doping on the Morphology and Electrochemical Performance of High-Voltage Spinel $LiNi_{0.5}Mn_{1.5}O_4$ Cathode Material. *ACS Appl. Mater. Interfaces* **2016**, *8*, 9116–9124. [CrossRef] [PubMed]
40. Mohamedi, M.; Makino, M.; Dokko, K.; Itoh, T.; Uchida, I. Electrochemical investigation of $LiNi_{0.5}Mn_{1.5}O_4$ thin film intercalation electrodes. *Electrochim. Acta* **2002**, *48*, 79–84. [CrossRef]
41. Rahim, A.S.A.; Kufian, M.Z.; Arof, A.K.M.; Osman, Z. Variation of Li Diffusion Coefficient during Delithiation of Spinel $LiNi_{0.5}Mn_{1.5}O_4$. *J. Electrochem. Sci. Technol.* **2022**, *13*, 128–137. [CrossRef]
42. Sarkar, T.; Prakasha, K.R.; Bharadwaj, M.D.; Prakash, A.S. Lithium diffusion study in Li_2MnO_3 and $Li_{1.17}Ni_{0.17}Mn_{0.67}O_2$: A combined experimental and computational approach. *Phys. Chem. Chem. Phys.* **2017**, *19*, 31724–31730. [CrossRef]
43. Gellert, M.; Gries, K.I.; Sann, J.; Pfeifer, E.; Volz, K.; Roling, B. Impedance spectroscopic study of the charge transfer resistance at the interface between a LiNi0.5Mn1.5O4 high-voltage cathode film and a LiNbO3 coating film. *Solid State Ionics* **2016**, *287*, 8–12. [CrossRef]
44. Viswanathan, V.V.; Choi, D.; Wang, D.; Xu, W.; Towne, S.; Williford, R.E.; Zhang, J.G.; Liu, J.; Yang, Z. Effect of entropy change of lithium intercalation in cathodes and anodes on Li-ion battery thermal management. *J. Power Sources* **2010**, *195*, 3720–3729. [CrossRef]
45. Marcicki, J.; Yang, X.G. Model-Based Estimation of Reversible Heat Generation in Lithium-Ion Cells. *J. Electrochem. Soc.* **2014**, *161*, A1794–A1800. [CrossRef]
46. Shi, W.; Zheng, J.; Xiao, J.; Chen, X.; Polzin, B.J.; Zhang, J.G. The Effect of Entropy and Enthalpy Changes on the Thermal Behavior of Li-Mn-Rich Layered Composite Cathode Materials. *J. Electrochem. Soc.* **2016**, *163*, A571–A577. [CrossRef]
47. Mao, J.; Zhang, P.; Liu, X.; Liu, Y.; Shao, G.; Dai, K. Entropy Change Characteristics of the $LiNi_{0.5}Mn_{1.5}O_4$ Cathode Material for Lithium-Ion Batteries. *ACS Omega* **2020**, *5*, 4109–4114. [CrossRef]
48. Sayah, S.; Baazizi, M.; Karbak, M.; Jacquemin, J.; Ghamouss, F. Deep and Comprehensive Study on the Impact of Different Phosphazene-Based Flame-Retardant Additives on Electrolyte Properties, Performance, and Durability of High-Voltage LMNO-Based Lithium-Ion Batteries. *Energy Technol.* **2023**, *11*, 2201446. [CrossRef]

49. Baazizi, M.; Sayah, S.; Karbak, M.; Hajjaj, O.; Aqil, M.; Dahbi, M.; Ghamouss, F. Revealing the Influence of Electrolyte Additives in Reducing the Heat Generation of High Voltage Lithium-Ion Batteries using Operando Accelerating Rate Calorimetry (ARC). *Batter. Supercaps* **2023**, *6*, e202300151. [CrossRef]
50. Jalkanen, K.; Aho, T.; Vuorilehto, K. Entropy change effects on the thermal behavior of a $LiFePO_4$/graphite lithium-ion cell at different states of charge. *J. Power Sources* **2013**, *243*, 354–360. [CrossRef]
51. Jalkanen, K.; Vuorilehto, K. Entropy change characteristics of $LiMn_{0.67}Fe_{0.33}PO_4$ and $Li_4Ti_5O_{12}$ electrode materials. *J. Power Sources* **2015**, *273*, 351–359. [CrossRef]
52. Schlueter, S.; Genieser, R.; Richards, D.; Hoster, H.E.; Mercer, M.P. Quantifying structure dependent responses in Li-ion cells with excess Li spinel cathodes: Matching voltage and entropy profiles through mean field models. *Phys. Chem. Chem. Phys.* **2018**, *20*, 21417–21429. [CrossRef]
53. Yun, F.l.; Jin, W.r.; Tang, L.; Li, W.; Pang, J.; Lu, S.g. Analysis of Capacity Fade from Entropic Heat Coefficient of $Li[Ni_xCo_yMn_z]O_2$/Graphite Lithium Ion Battery. *J. Electrochem. Soc.* **2016**, *163*, A639–A643. [CrossRef]
54. Böhm, K.; Zintel, S.; Ganninger, P.; Jäger, J.; Markus, T.; Henriques, D. Exploring the Impact of State of Charge and Aging on the Entropy Coefficient of Silicon–Carbon Anodes. *Energies* **2024**, *17*, 5790. [CrossRef]
55. Patoux, S.; Sannier, L.; Lignier, H.; Reynier, Y.; Bourbon, C.; Jouanneau, S.; Le Cras, F.; Martinet, S. High voltage nickel manganese spinel oxides for Li-ion batteries. *Electrochim. Acta* **2008**, *53*, 4137–4145. [CrossRef]
56. Wu, Q.; Zhang, X.; Sun, S.; Wan, N.; Pan, D.; Bai, Y.; Zhu, H.; Hu, Y.S.; Dai, S. Improved electrochemical performance of spinel $LiMn_{1.5}Ni_{0.5}O_4$ through MgF_2 nano-coating. *Nanoscale* **2015**, *7*, 15609–15617. [CrossRef] [PubMed]
57. Talyosef, Y.; Markovsky, B.; Salitra, G.; Aurbach, D.; Kim, H.J.; Choi, S. The study of $LiNi_{0.5}Mn_{1.5}O_4$ 5-V cathodes for Li-ion batteries. *J. Power Sources* **2005**, *146*, 664–669. [CrossRef]
58. Oney, G.; Sevillano, J.S.; Yahia, M.B.; Olchowka, J.; Suard, E.; Weill, F.; Demortière, A.; Cabanas, M.C.; Croguennec, L.; Carlier, D. Identification of degree of ordering in spinel LiNi0.5Mn1.5O4 through NMR and Raman spectroscopies supported by theoretical calculations. *Energy Storage Mater.* **2024**, *70*, 103486. [CrossRef]
59. Heubner, C.; Schneider, M.; Michaelis, A. Heat generation rates of $NaFePO_4$ electrodes for sodium-ion batteries and $LiFePO_4$ electrodes for lithium-ion batteries: A comparative study. *J. Solid State Electrochem.* **2017**, *22*, 1099–1108. [CrossRef]

Disclaimer/Publisher's Note: The statements, opinions and data contained in all publications are solely those of the individual author(s) and contributor(s) and not of MDPI and/or the editor(s). MDPI and/or the editor(s) disclaim responsibility for any injury to people or property resulting from any ideas, methods, instructions or products referred to in the content.